Paper Skin Multisensory Platform for Simultaneous Environmental Monitoring

*Joanna M. Nassar, Marlon D. Cordero, Arwa T. Kutbee, Muhammad A. Karimi, Galo A. Torres Sevilla, Aftab M. Hussain, Atif Shamim, and Muhammad M. Hussain**

Human skin and hair can simultaneously feel pressure, temperature, humidity, strain, and flow—great inspirations for applications such as artificial skins for burn and acid victims, robotics, and vehicular technology. Previous efforts in this direction use sophisticated materials or processes. Chemically functionalized, inkjet printed or vacuum-technology-processed papers albeit cheap have shown limited functionalities. Thus, performance and/or functionalities per cost have been limited. Here, a scalable "garage" fabrication approach is shown using off-the-shelf inexpensive household elements such as aluminum foil, scotch tapes, sticky-notes, napkins, and sponges to build "paper skin" with simultaneous real-time sensing capability of pressure, temperature, humidity, proximity, pH, and flow. Enabling the basic principles of porosity, adsorption, and dimensions of these materials, a fully functioning distributed sensor network platform is reported, which, for the first time, can sense the vitals of its carrier (body temperature, blood pressure, heart rate, and skin hydration) and the surrounding environment.

1. Introduction

Paper is a universally widespread material that is available in every household due to its low cost and necessity for everyday use. One of the advantages of using paper substrates for sensors applications is its porosity and its larger interfacial area that promotes both high sensitivity and fast response. To date, several works have used paper as a host platform or a sensing material for building various types of devices, ranging from flexible actuators, to displays and paper-based micro-electromechanical system (MEMS) electronics, such as ammonia gas sensors, multi-color LED displays, 3D antennas, cantilever-type MEMS deflection sensors and foldable thermochromic displays on paper.[1–6] Advancements in the field of paper electronics are rapidly growing due to the low-cost and recyclable benefits of paper, where major focus has been directed toward using flexible cellulose paper for the fabrication of various types of sensors, such as humidity, touch, pH, and gas sensors.[7–10] However, these approaches still use sophisticated and often expensive nanomaterials-based functionalization, vacuum manufacturing processes, and printing techniques, where paper is still often chemically treated and solution-processed.[11–13]

Flexible artificial skin advances have also paved their way in the literature, aiming for soft skins for robotic applications through the means of pressure and temperature sensors integrated on polyethylene terephthalate (PET) or polyimide (PI) substrates.[14–19] However, the existing approaches are still far from being commercialized due to their fairly expensive manufacturing processes and complex integration. Although flexible plastic substrates are relatively cheap (PET ≈ 2 cents dm^{-2} and PI ≈ 30 cents dm^{-2}), the price of paper is substantially lower (≈0.1 cent dm^{-2}).[6] Developments in artificial skin integration have shown possibilities for strain, humidity, pressure, and temperature sensing.[20–31]

In this work, we show a far cheaper alternative to the widespread artificial skin systems, using paper-based sensors and "ridiculously" common fabrication tools: scissors and tape. We have not functionalized or treated the paper in any way, nor used any microfabrication processes such as sputtering, shadow mask, or solution-etching techniques. Our simple fabrication process is aimed for household manufacturing of the sensors, making them accessible for anyone at any age and regardless of financial status.

We demonstrate the first ever recyclable 3D stacked 6 × 6 "Paper Skin" array for simultaneous sensing, integrated solely from household resources such as paper, 3M adhesive tape, aluminum/copper foil, kitchen sponge, tissue fabric (napkins), and pencil. Although aluminum foil is sufficient for interconnects and contacting pads, we have also used a silver conducive ink pen "Circuit Scribe," for scalability and arraying purposes.

J. M. Nassar, M. D. Cordero, A. T. Kutbee, G. A. T. Sevilla, A. M. Hussain, Prof. M. M. Hussain
Integrated Nanotechnology Lab
Computer Electrical Mathematical Science and Engineering Division
King Abdullah University of Science and Technology (KAUST)
Thuwal 23955-6900, Saudi Arabia
E-mail: muhammadmustafa.hussain@kaust.edu.sa

M. A. Karimi, Prof. A. Shamim
IMPACT Lab
Computer Electrical Mathematical Science and Engineering (CEMSE) Division
King Abdullah University of Science and Technology (KAUST)
Thuwal 23955-6900, Saudi Arabia

DOI: 10.1002/admt.201600004

We used off-the-shelf materials to fabricate and integrate the following sensors: pressure, temperature, humidity, pH, and flow sensors including tactile and proximity detection.

Unlike artificial skin platforms aiming for high-end sensitivities, our objective is to develop a low-cost, eco-friendly, and multifunctional paper-based sensors network, providing sufficient functionality and ease of access to monitoring and awareness systems. The ability to detect pressure, tactile, proximity, and motion positions could enable more intuitive human–computer interactions, in a much more accessible way than we imagined. The paper skin can be envisioned in various household and healthcare applications, ranging from food quality examination to atmospheric monitoring, basic real-time symptoms, and illness detection.

2. Design and Operation

For sensors design, a 3M Post-it Note is used as a flexible paper substrate, and aluminum foil and silver ink pen are used for the contact pads and interconnects. A spectrum of materials and structures are used for the sensing film to achieve the desired performance and application. Table S1 (Supporting Information) shows the list of materials used for each specific sensor, highlighting their important characteristics. Both temperature and pH sensors have a resistive functionality, whereas both humidity and pressure sensors rely on a capacitive-based sensing. Detailed design and process flow of the sensors are illustrated in **Figure 1** and discussed in the Experimental Section. In the following sections, we present the details of every sensor's principle of operation and choice of material.

2.1. Temperature Sensors

Temperature sensor is either cut out of aluminum foil or drawn with the silver conductive pen on the Post-it paper (Figure 1a). The aluminum foil has an electrical resistivity of 3.83×10^{-8} Ω m, whereas the silver pen on paper has a resistivity in the interval of 0.05–0.2 Ω □$^{-1}$. This slight variation in the electrical conductivity is due to the variability in filling density. The resistance of the sensor will vary with temperature due to phonon vibrations in the lattice structure of the metal, which will increase the spacing between atoms and reduce the ability of the material to properly conduct the electrical current, causing an increase in resistance. The relative resistance change versus temperature f(T) = $\Delta R/R$ of temperature resistors is commonly represented by the value of the temperature coefficient of resistance (TCR). The TCR is defined as the slope of the $\Delta R/R$ = f(T) curve and can be expressed by

$$\mathrm{TCR} = \left(\frac{\Delta R}{\Delta T}\right)/R \tag{1}$$

where TCR [in °C^{-1}], ΔR [in Ω] is the change in resistance corresponding to ΔT [in °C] the change in temperature, and R [in Ω] is the initial resistance of the sensor. The theoretical TCR of silver and aluminum at 20 °C are, respectively, 0.0038 and 0.0039 °C^{-1}.[32]

2.2. Humidity Sensor

For the capacitive humidity sensors (Figure 1b), paper withholds an advantageous property for measuring humidity due to its porous cellulose-fiber nature, and the adsorption and desorption of moisture on paper relative to humidity levels are a well-known phenomenon.[6,33] Since paper is hygroscopic, as humidity level increases, more water molecules adsorb to the hydroxyl groups on the surface of the paper, changing the relative permittivity and altering in turn the capacitance of the sensor. Water has a relative permittivity of $\varepsilon_{r,water} = 80.1$ at 20 °C, thus the permittivity of paper is expected to increase, leading to an increase in capacitance as humidity levels rise (Equation (2))

$$C = \varepsilon_0 \varepsilon_r A/d \tag{2}$$

where C is the capacitance of the sensor [in F], ε_0 is the vacuum permittivity ($\varepsilon_0 \approx 8.854 \times 10^{-12}$ [F m^{-1}]), ε_r is the relative permittivity of the dielectric material in between the two conductive fingers, and d is the separation between the parallel conductive plates [in m]. As an optional step for stability in measurement fluctuations, we have covered the sensor structure with a sheet of KIMTECH wipe, which shows to reduce electrical discharges and has a relative permittivity very close to that of air (Table S1, Supporting Information).

2.3. PH Sensor

For the pH sensor, pencil of grade HB acts as the sensing film (Figure 1c). It has 68% carbon and 26% clay,[34] and the electrical resistivity is calculated to be $\rho = 1.85 \times 10^{-4}$ Ω m. Note that ρ is highly dependent on the content of carbon, and decreases as the percentage of carbon increases.[34] The principle of operation relies on measuring the change in resistance upon exposure to different pH levels. Since paper substrate is sensitive to moisture, once exposed to a solution (regardless of the pH level), moisture level in the paper will increase and saturate increasing the electrical conductivity of the paper and inducing a change in the resistance of the sensor. In fact, resistance of paper was found to decrease with water molecules adsorbed on its surface. Pure water should be an excellent insulator; however, water undergoes autoionization in the liquid state when two water molecules form one hydroxide anion (OH^-) and one hydronium cation (H_3O^+). And since water is a great solvent, it often has some tiny impurities dissolved in it (e.g., salt), which can conduct electricity.[35] To prove this statement, we test the resistance of our pH structure without the graphite film on top, and we measure resistance before and after putting it in contact with water. With no water, the resistance is measured to be $R_{paper} = 258$ MΩ, and with added water the resistance decreases to $R_{paper+water} = 1.07$ MΩ. This translates into a total decrease in the structure resistance by 256.93 MΩ. This test shows that the resistance contributed by the soaked paper is very high, and thus in the case of PH sensing, the electrical current will favorably choose the more conductive path which is through the conductive graphite film, making it clear that the dampened paper's contribution to conductivity is negligible. This being said, we consider this resistivity dependence on humidity to

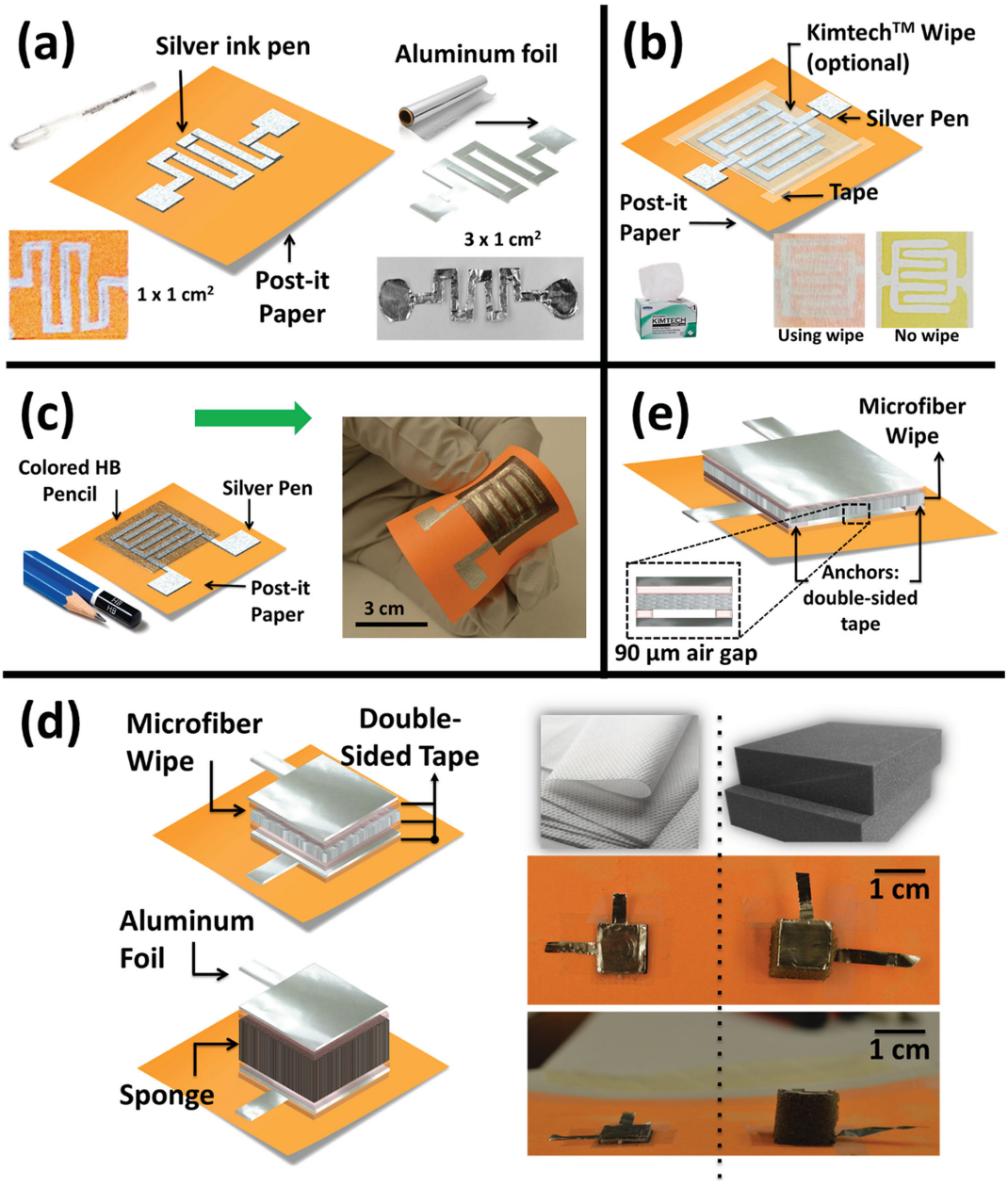

Figure 1. a) Schematic of temperature sensors using silver ink pen and aluminum foil. b) Capacitive design of humidity sensor using post-it paper as sensing material. c) Representation of a capacitive-based disposable pH sensor. d) "Design 1" of pressure sensors using a parallel-plate structure and two different sensing materials: microfiber wipe and a sponge. e) Schematic of "Design 2" of pressure sensor based on air-gap structure.

be negligible compared to the high conductivity introduced by the pencil layer and constant for all solutions under study. In this case, the dominant effect is the redox reaction occurring between the graphite and hydroxyl ions in the corresponding aqueous solutions.[36] An acidic solution has higher concentration of hydrogen ions H^+ than water, and a basic solution has higher concentration of hydroxide ions OH^-. The sensing mechanism can be explained by the adsorbed ions (hydroxonium ions H_3O^+ and hydroxyl ions OH^-). When exposed to an alkaline solution, the carbonyl functional group goes through a reduction step (gaining electrons e^-), eventually transforming into methane (CH_4) the most highly reduced state, decreasing the resistance with respect to neutral solution resistance. Conversely, when exposed to an acidic solution, the carbon-based film goes through an oxidation step (loses e^-), eventually becoming CO_2, which is the most highly oxidized state, increasing the measured sensor's resistance.[36]

2.4. Multifunctional Force Sensor

Principle of operation of pressure sensors (Figure 1d) is described in Equation (2). As applied pressure increases, the dielectric thickness decreases, increasing the output capacitance

of the sensor. In fact, due to the elastic deformation and porous properties, the sponge will vary in thickness as it is exposed to various external forces. Similarly, the cleanroom wipes are composed of multilayer microfiber construction; this texture allows for high sensitivity and deformation under mechanical stimuli. In order to further improve the sensor's response to lower pressure regimes, an air-gap-based design was implemented (Figure 1e). This geometry allows detection of lower pressure due to the ultrahigh compressibility of air. In fact, it has been shown that electrical signals from vibrations are dramatically amplified when an air gap of few micrometers in size is implemented in the sensor's structure.[37]

2.5. Paper Skin Integration

Finally, we build a 6 × 6 artificial paper skin through the superposition of three layers of sensor networks, as shown in **Figure 2**. Details about the array design are described in the Experimental Section. The pressure-sensing platform provides multifunctionality for force, touch, motion, direction, and proximity sensing due to its unique structure illustrated in the cross-sectional photograph in Figure 2d, with a focus onto its air gap shown in Figure 2e. This stacking configuration allows for simultaneous localized sensing of various external stimuli per pixel, bringing together extensive sensing functionalities in a low-cost and sustainable manner.

3. Materials Characterization and Discussion

Thickness, electrical resistivity, and relative permittivity are the essential material properties required to build our devices and understand their behavior. These characteristics are summarized in Table S1 (Supporting Information). Thickness was obtained through a high-accuracy digital micrometer; electrical resistivity using a four-point probe resistivity measurement, and relative permittivity was calculated from the measured capacitance of a 3 × 1 cm^2 capacitor, using the studied material as the dielectric.

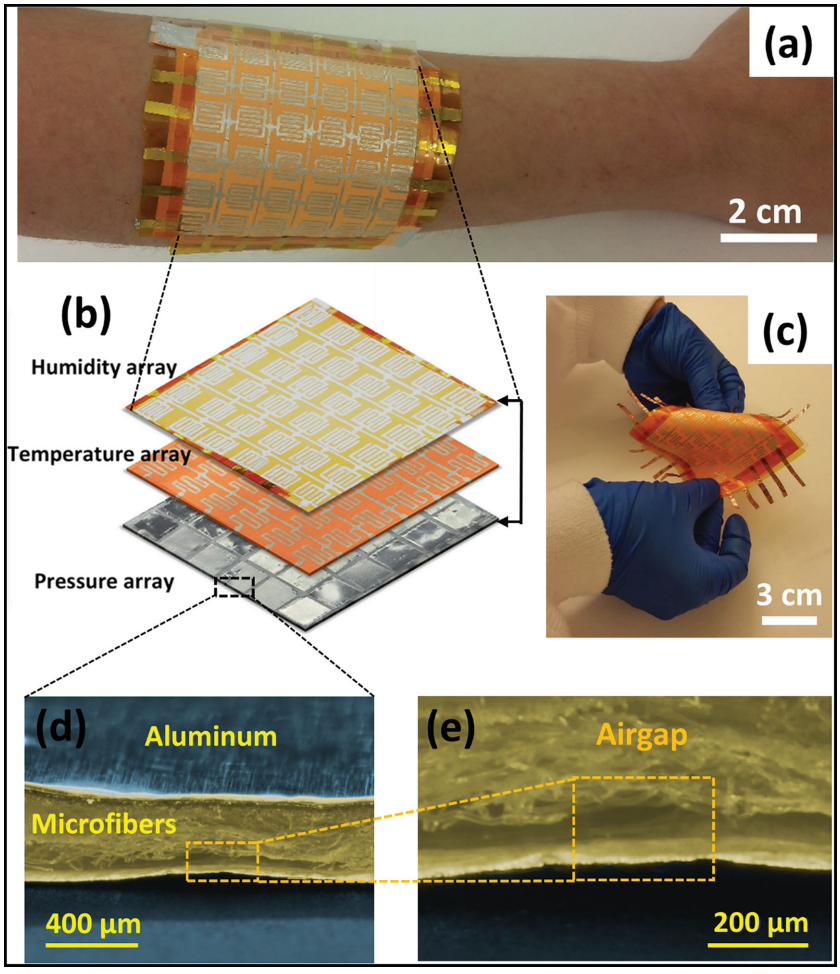

Figure 2. a) Digital photograph of flexible 6 × 6 "paper skin" wrapped around an arm. b) Schematic of 3D stacked paper skin structure composed of pressure, temperature, and humidity arrays. c) Digital photograph of flexible temperature sensors array. d) High-resolution photograph of the cross-section of the pressure sensor "design 2," showing the microfiber wipe sandwiched in aluminum foil with an air-gap cavity. e) Zoom in picture of the air-gap assembly.

3.1. Topography and Porosity of Household Materials

Scanning electron microscopy (SEM) was performed to study the surface topography and porosity of the different materials. For sample preparation of the post-it note, the piece of paper was blow-dried with nitrogen (N_2) to remove dust particles, and then coated with 2 nm layer of Iridium (Ir) to prevent charging during imaging. The SEM image in **Figure 3**a reflects the fiber structure of the post-it paper through the apparent mesh of cellulose microfibrils. Cellulose is hydrophilic and insoluble in water, which makes it perfect for our humidity sensing purposes. As for the sponge and the microfiber cleanroom wipe, the samples were sputtered with a 2 nm layer of Ir to prevent charging. SEM images in Figure 3b,c confirm the porous nature of our chosen materials. This porosity allows more compressibility and deformation; an advantageous property for improved low-pressure sensitivity.[38] We notice that the sponge exhibits a different structure than the cleanroom wipe, where it displays a network of hallow hexagonal microstructures (pores), whereas the polypropylene (PP) wipe illustrates a network of randomly oriented microfibril threads. As shown in Figure 3c, the wipe reveals low density of microfibrils, translating into higher sensitivity to small loads. In fact, the synthetic sponge is made out of foamed polyester (PES), which is rugged, stiffer, and has higher density than the PP found in the cleanroom wipes (D_{PP} = 0.91 g cc^{-1}; D_{PES} = 1.38 g cc^{-1}).[39] Besides,

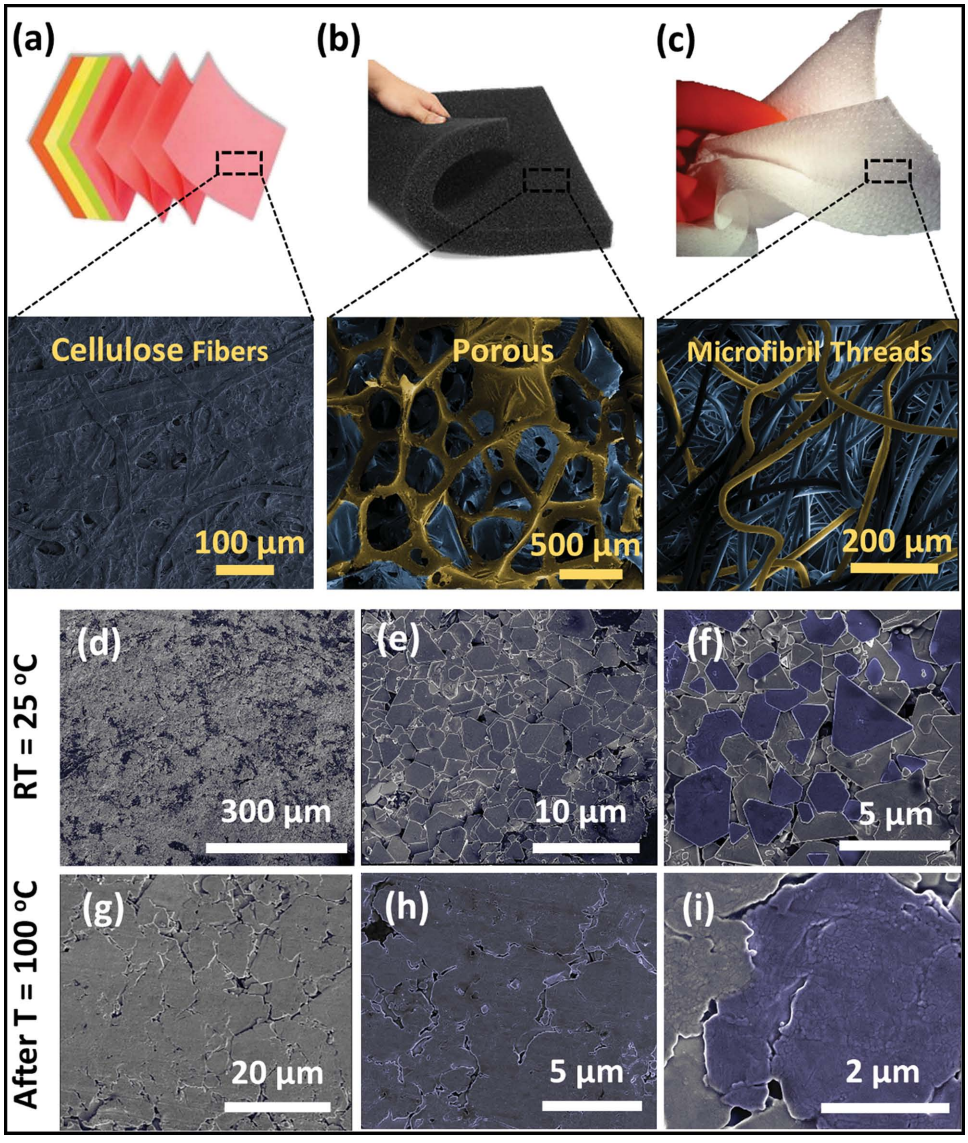

Figure 3. Optical and scanning electron microscopy (SEM) images highlighting the different porosity structures and topographies of a) Post-it paper, b) sponge, c) and cleanroom microfibril wipe. All materials were coated with 2 nm of Iridium (Ir). d–f) SEM images of silver (Ag) ink on post-it paper drawn at room temperature. g–i) SEM images of the same silver ink sheet after heating at 100 °C and left to cool down at room temperature.

elongation is much higher for PP, which gives better elasticity and thus more compressibility. Therefore, it is expected that the cleanroom wipe-based sensor will demonstrate a higher sensitivity to pressure, whereas the sponge-based sensor will show a wider range of operation in the high pressure regime, due to its larger thickness.

3.2. Interconnects Stability

Since silver ink was used for designing temperature sensors and integration networks, we study the stability of the silver ink interconnects at high temperatures. We perform SEM of a silver ink sheet on top of the post-it paper, before and after heating the sample to 100 °C. Resistance values were extracted for both cases only after the temperature of the surface came back to room temperature (T = 25 °C). Figure 3d–f shows the SEM images of the silver (Ag) ink particles before heating, where we can clearly distinguish the fairly uniform distribution of Ag hexagonal microstructures. After heating to 100 °C, room temperature images in Figure 3g–i indicate that the silver-based gel-ink pen has expanded and the enlarged Ag microstructures have superimposed. The diffusion temperature of pure Ag is determined to be above 630 °C;[40] however the circuit scribe conductive pen composition is like that of any commercial gel-ink pen, except the color pigments in the pen have been replaced by silver particles. This being said, a gel medium exhibits a high liquid viscosity, described by the dynamic viscosity (μ), where the viscosity of the medium tends to decrease as temperature increases, translating into a liquefied medium that promotes the superposition of Ag particles. The dynamic viscosity (μ) is

exponentially dependent on temperature by Reynolds' model by Equation (3)

$$\mu(T) = \mu_0 \, e^{-bT} \tag{3}$$

where T is temperature [in °C], μ is the viscosity of the liquid [in Pa s] and μ_0 and b are empirical coefficients of the model. Moreover, at elevated temperatures, the silver particles have undergone thermal expansion in which their volume expands in response to temperature through heat transfer. The volumetric thermal expansion coefficient α_v of any medium is described by Equation (4)

$$\alpha_V = \frac{1}{V}\left(\frac{\partial V}{\partial T}\right)_p \tag{4}$$

where V is the medium's volume [m^3], T is the temperature [K], and p indicates that the pressure is held constant during expansion. The linear thermal expansion coefficient of silver is $\alpha_{Ag} = 18 \times 10^{-6}$ K^{-1}[41] and since silver is an isotropic material, then the area thermal expansion coefficient becomes $2\alpha_{Ag}$ and the volumetric expansion coefficient is $3\alpha_{Ag}$. The results display an irreversible process where the sheet resistance of silver ink interconnects decreases due to an improvement in film density. Figure S1 (Supporting Information) illustrates the decrease in resistance after the silver ink is heated to temperatures up to 100 °C. Resistance decreases from 4.75 Ω at room temperature (25 °C) down to 2.83 Ω after heating to ≈95 °C, given that the resistance value was taken after the conductive ink cooled down to room temperature.

4. Performance Analysis and Discussion

4.1. Sensitivity and Real-Time Study of Temperature Detection

First, we evaluate the temperature sensor behavior, comparing the silver-ink-based sensor with the aluminum-foil-based sensor. In this case, the silver-ink-based sensor was used after it was heated to 100 °C and cooled down to insure material stability. Then, we characterize each sensor on a thermal chuck probe station, where the chuck is heated from 25 °C up to 100 °C with steps of 10 °C. For precision, the temperature on the surface of the sensor is measured using a thermocouple and the resistance value is collected using a digital multimeter. Figure S2 (Supporting Information) shows that both sensors exhibit a linear behavior where resistance increases with respect to temperature. The calculated TCR for aluminum foil and silver ink pen are, respectively, $TCR_{exp,Al} = 0.00383$ °C^{-1} and $TCR_{exp,Ag} = 0.00372$ °C^{-1}. Our experimental values very closely match the materials' theoretical TCR values of $TCR_{th,Al} = 0.0039$ °C^{-1} with a relative %error of 1.8% and $TCR_{th,Ag} = 0.0038$ °C^{-1} with a relative %error of 2.1%.[32] We show that the silver-ink-based sensor is nine times more sensitive than the aluminum-foil-based temperature sensor, with respective sensitivities of $S_{Ag} = 0.0107$ Ω °C^{-1} and $S_{Al} = 0.00115$ Ω °C^{-1}.

For arraying purposes, we continue our studies with the silver-ink-based sensor. We perform temporal study measurements, where we exposed the sensor to very common external stimuli that we encounter in everyday life. We test the temperature sensor's real-time response to human touch ($T = 37$ °C) (**Figure 4**a,b), human exhaled breath (around 42 °C) (Figure 4c,d), and from a lighter flame positioned 10 cm away from the sensor ($T \approx 85$ °C) (Figure 4e). Figure S3a (Supporting Information) shows the Gaussian/Lorentzian profile of the sensor's response to human touch. The maximum change in voltage is $\Delta V = 1.38$ mV corresponding to a change in temperature of $\Delta T = 12$ °C relative to room temperature. The total response time of the sensor is 7.37 s and the total time for the sensor to recover its initial state is 10.32 s. The recovery takes the shape of an exponential decay from which we can retrieve the rate of decay by extracting the mean lifetime τ or half-life $t_{1/2}$ of the sensor, corresponding to the time required for the sensor to fall back to half of its initial value. In this case, the half-life of the sensor was determined to be $t_{1/2} = 1.88$ s. For breath temperature detection (Figure S3b, Supporting Information), the maximum change in voltage is $\Delta V = 2.34$ mV corresponding to a change in temperature of $\Delta T = 20$ °C relative to room temperature. The sensor exhibits a spike response time of 421 ms, with a total recovery time of 7.16 s. For the final test, we position the flame of a lighter about 10 cm away from the surface of the sensor. Figure S3c (Supporting Information) shows the originated change in voltage in response to the flame's heat. The peak change recorded is $\Delta V = 6.59$ mV corresponding to $\Delta T = 60$ °C. The total response time is about 1.89 s, with the fastest total recovery time of 5.27 s.

Our paper-based temperature sensors show high sensitivity to the point of detecting the spectroscopic behavior of the exhaled breath (Figure 4d). This signal originates from the pulsating nature of our breathing process, controlled by our heart rate.[42] We report ultrafast response and recovery times of 421 ms and 5.27 s, respectively, compared to 20 s response and 30 s recovery time reported in the previously published literature.[43]

4.2. Moisture Recognition and Time Study of Humidity Sensing

We study the behavior of the humidity sensor by exposing it to three different values of known humidity levels: room temperature (46%), human breath (76%), and water vapor (97%). These humidity values were determined using a commercial humidity sensor. As expected, Figure S4a (Supporting Information) shows a nearly linear increase in the capacitance as humidity levels increase. The maximum calculated sensitivity is 0.18%/% RH, which is quite low compared to values reported in the literature,[44,45] but still we show a very repeatable behavior with fast adsorption and desorption times.

Humidity in the surrounding environment was led in real-time for different external stimuli shown in Figure 4g–j. The experimental setups are clarified in the Experimental Section, and shown in Figure 4g,h for the water vapor test. For humid breath testing, Figure 4i shows an increase of 0.025 pF in capacitance as a response to 76% relative humidity. Figure S4b (Supporting Information) shows a very fast total response time of 2 s, with an exceptional growth behavior with half-life time $t_{1/2} = 0.34$ s. As for the recovery of the sensor, desorption follows a Boltzmann profile, with total recovery time of 1.33 s. For damp weather detection, we use a water vapor setup, where the time study in

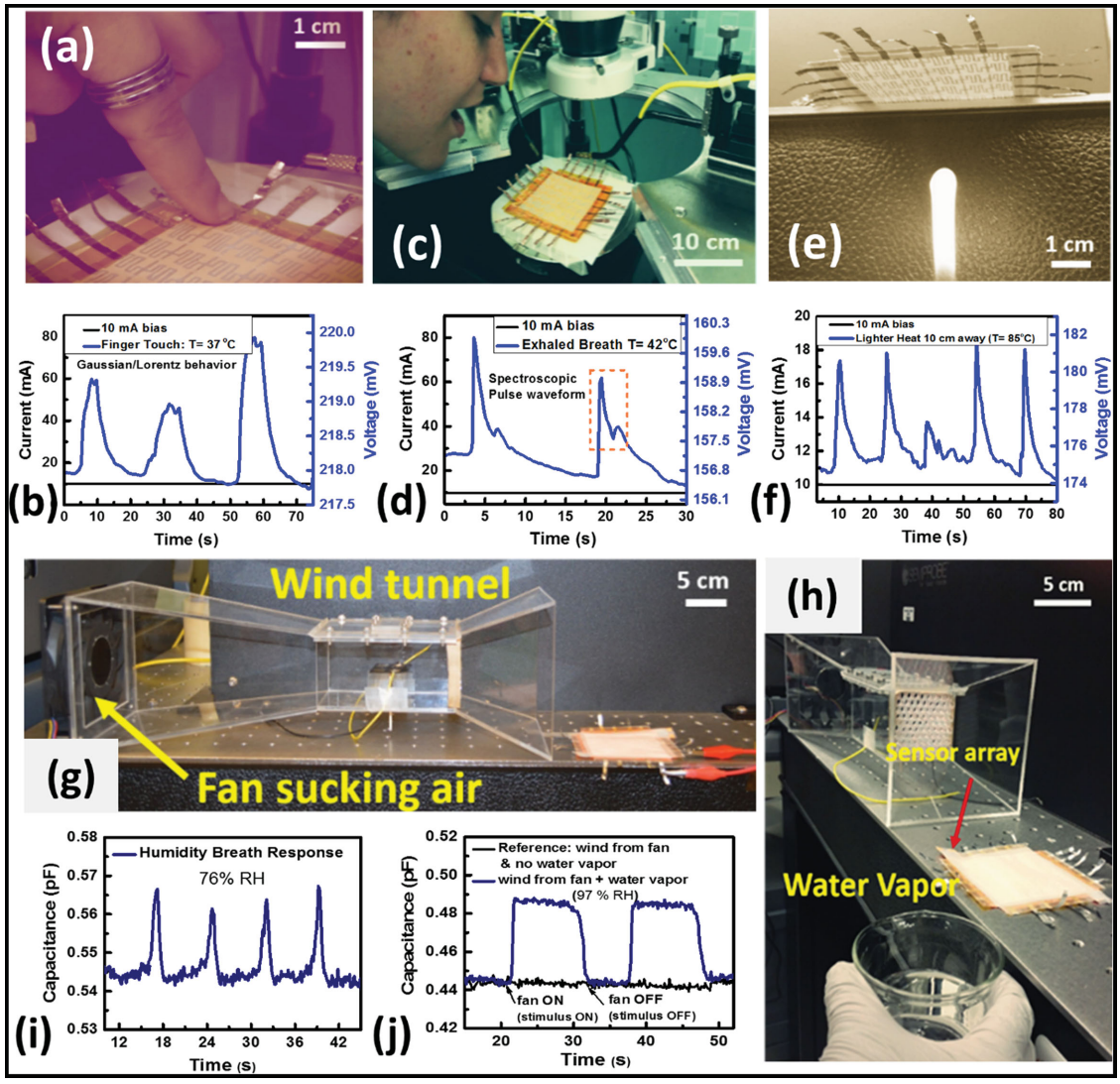

Figure 4. a) Optical image showing external stimuli from human touch, exerting a temperature of around $T = 37$ °C. b) Real-time temperature response to human touch, for three consecutive cycles. c) Digital photo of external stimuli from human exhaled breath (around 42 °C). d) Real-time temperature response for two cycles of exhaled breath over a period of 30 s. e) Image showing external stimulus exerted from the flame of a lighter ($T = 85$ °C), positioned 10 cm away from the surface of the sensor. f) Real-time response for five cycles of applied stimuli over a period of 80 s. g,h) Photographs illustrating the wind tunnel setup used to uniformly apply water vapor on top of the humidity sensor array. i) Real-time response to humidity levels detected from four cycles of human breath. h) Real-time humidity profile showing a positive response toward water vapor detection.

Figure 4i demonstrates that the activation of the wind tunnel fan has no effect on the response of our sensor, guaranteeing that the behavior seen is solely from the vapor humidity. In this case, the sensor has a total response time of 1.2 s and a recovery time of 3.2 s (Figure S4c, Supporting Information). Typically, although the sensitivity reported is not so high, however we report very fast response and recovery times of ≈1 s and 1.33 s, respectively, nearly ten times faster than the ones found in the literature using complex fabrication processes and expensive materials.[46–48]

The observed faster response and recovery times are respectively attributed to faster absorption and evaporation rates in porous surfaces (e.g., cellulose paper in this work) in contrast to the flat nonporous materials commonly used in the literature. The faster absorption in porous media is driven by the capillary pressure, which is inversely proportional to the pore size, but also the permeability of porous materials scales with the square of the pore size.[49] Thus, this dynamic superimposition of both mechanisms for liquid absorption leads to an overall faster absorption time in heterogeneous porous structures.[49] In this case, the absorption time can be expressed either by the classic Washburn's Law for simple porous constructs (Equation (5)),[49,50] or by Darcy's law (Equation (6))[51] for a more accurate representation of the absorption process of water in a heterogeneous porous medium:

$$z = (Dt)^{0.5} \text{ with } D = \frac{\gamma r \cos\theta}{2\eta} \tag{5}$$

$$u = -\frac{K}{\eta}\nabla p \tag{6}$$

where D is the diffusion coefficient of the liquid, γ and η, respectively, represent the liquid–vapor surface tension and the viscosity of the liquid, r is the tube radius of the pores model, and θ is the contact angle characterizing the wetting of the liquid on the wall of the tube. As for Equation (6), K is the permeability tensor of the medium, ∇p is the pressure gradient, and u is the flow velocity. Further details about the different models generated to study these phenomena are described in the following literature.[49–51]

As for evaporation, the overall evaporation rate is determined by the combined effects of vapor transport through the pore network and subsequently into the air. In fluid mechanics models, evaporation is described exclusively in terms of mass transfer.[52] In this manner, evaporation occurs faster in a porous medium than a flat surface due to an increased contact area on the perimeter between the water droplet and the porous surface (spreading effect).[52] In fact, the wetting of the liquid on a surface depends on the porosity of the surface. This effect is characterized by the spreading factor (S), which is the ratio of the diameter of the wet spot on the surface after impingement to the droplet diameter before impingement. Thus, for a water droplet, the mass change with time during evaporation as a function of droplet radius is expressed by Equation (7):[53]

$$\dot{m} = 4\pi r_i^2 \rho_{p,i} \dot{r}_i \tag{7}$$

where $\dot{m}$ is the mass transfer with time, r_i is the radius of the droplet, and $\rho_{p,i}$ is the corresponding density of the fluid. Since the droplet on a porous surface undergoes spreading, the radius of the drop is larger, thus leading to an increased rate of mass transport into air, also known as evaporation. Detailed explanations of the models can be found in the literature.[54,55]

4.3. Fast Disposable Procedure for Uncovering Solution Acidity

For pH sensor evaluation, we used three different solutions with distinct pH levels as follows: water (pH = 7), diluted baking soda solution (pH = 8.5), and Nescafé coffee (pH = 4.5), where pH values were collected using pH test strips. Plotting the current versus voltage plot for every solution, we retrieve the associated resistance value. We first measure the reference resistance of the sensor and then we drop 2 mL of studied solution on the pH sensing film. During experimentation, we notice that the paper absorbs all the fluid after some time and saturates. In that case, the sensor was not surviving two consecutive measurements. For accurate results, this procedure uses a disposable sensor, valid for one-time use only. Therefore, for testing purposes, we used three matching pH sensors and used each one of them for one testing solution. The initial reference resistance was recorded for each sensor (R_i), then the final resistance (R_f) was measured after solution exposure, and we evaluate the change in resistance $\Delta R_{pH} = |R_f - R_i|$ corresponding to a change in pH level. **Figure 5**a shows the plot of resistance versus pH level. The resistance shown is the average resistance calculated from the addition of ΔR_{pH} to a common reference resistance R_{ref}. The resistance, respectively, increases to 355 Ω at pH = 4.5 and decreases to 150 Ω at pH = 8.5, with respect to the reference resistance value at pH = 7. The decrease in resistance as pH level increases is in accordance with the behavior reported in the literature for graphite-based pH sensors.[56–58]

The reported pH sensor is a low-cost, disposable, and recyclable sensor. In the absence of pH test strips, this procedure shows to be fast, reliable, and easy to make in any circumstance. pH levels can be simply recognized with the demonstrated paper-based sensor, allowing us to reveal the potential hazard of an unknown solution in crucial situations. In this case, acknowledgment of an acid or a base solution will be identified and associated with either an increase or decrease in the reference resistance, compared to a neutral water solution.

4.4. Multifunctional 3D-Force Sensing Device

4.4.1. Comparing Pressure Sensitivity of Compressible Materials

We begin by evaluating the pressure sensing behavior of the sponge-based sensor versus the cleanroom wipe-based sensor (Figure 1d). The comparative results of pressure-sensing capabilities between sponge and cleanroom wipe materials are shown in Figure 5b. We observe two linear regimes where the pressure sensitivities in the low-pressure interval (0–190 Pa) are $S_{1,sponge}$ = 0.09 pF kPa^{-1} and $S_{1,wipe}$ = 0.5 pF kPa^{-1}, respectively, for the sponge and wipe-based sensor. As for the high-pressure regime above 200 Pa, $S_{2,sponge}$ = 0.045 pF kPa^{-1}, and $S_{2,wipe}$ = 0.15 pF kPa^{-1}. As predicted by our material analysis, the cleanroom wipe exhibits higher-pressure sensitivity due to its microfibril structure that is more sensitive to smaller deformations than the cellulose matrix structure of the sponge. In other words, the cleanroom wipe material shows to be more compressible than the sponge, thus having a smaller bulk modulus K in Pa. Compressibility is explained by the volume (V) of a given solid mass will be reduced to $V–\delta V$ when a force or pressure is uniformly exerted all over its surface. If the force per unit area (i.e., pressure) of surface increases from P to $P + \delta P$, the relationship between change of pressure and change of volume depends on the bulk modulus (K) of the material, and is expressed by Equations (8) and (9):

$$\text{Bulk modulus } (K) = \frac{\text{Change in pressure}}{\text{Volumetric strain}} \tag{8}$$

$$K = \frac{\delta P}{\delta V / V} \tag{9}$$

where P is the pressure applied in Pa, and V is the volume of the material in m^3. The reciprocal of the bulk modulus is called the compressibility of the substance.

Then, we tested both sensors for maximum load detection, and we observed that the sponge-based sensor had a larger window for high-pressure detections, with sensing capabilities up to around 90 kPa before saturation (Figure S5, Supporting Information). Whereas the cleanroom wipe-based sensor entered the saturation mode after around 9.7 kPa of applied

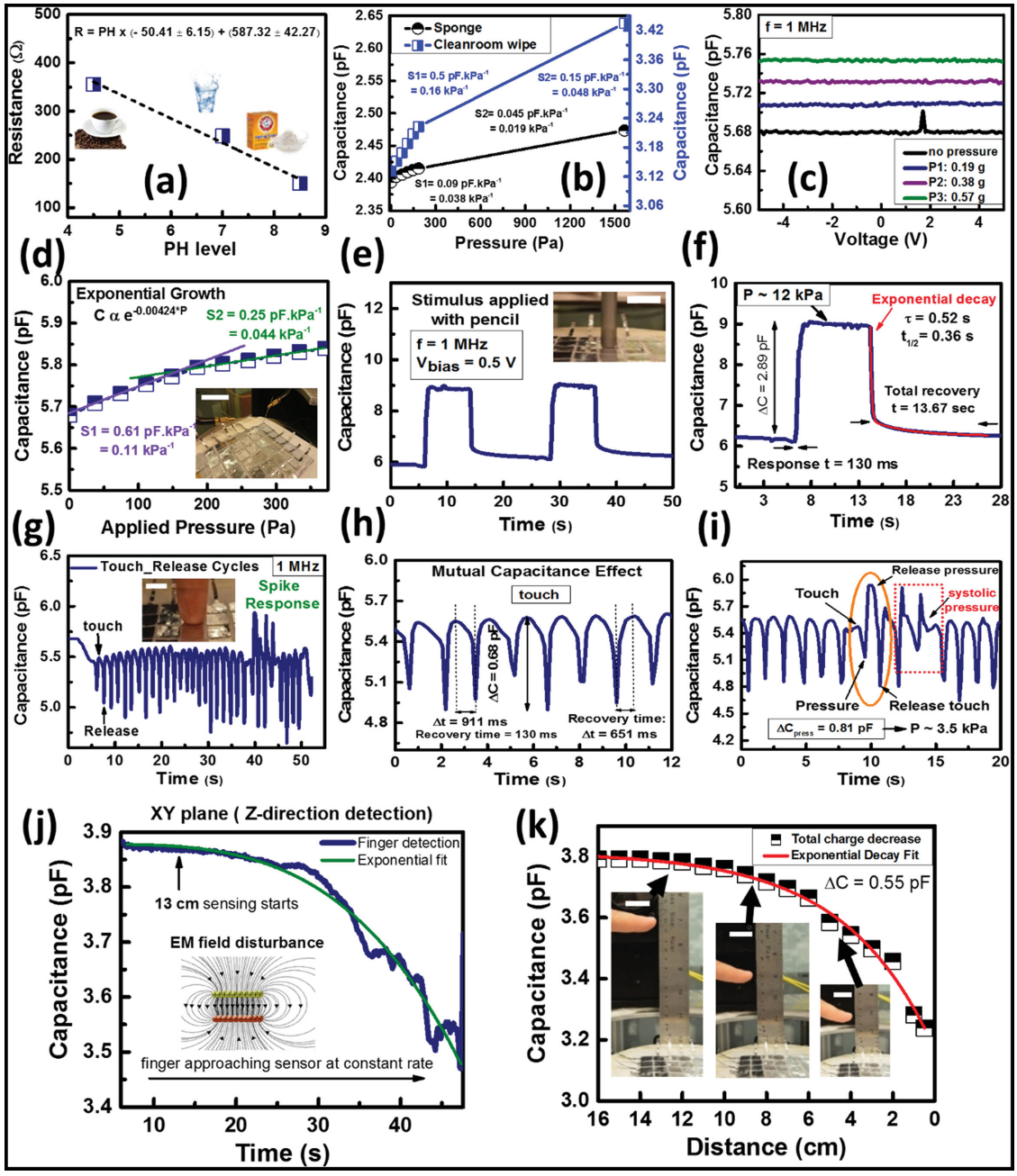

Figure 5. a) pH sensor performance using 2 mL of coffee, water, and baking soda solutions. b) Comparative study of pressure-sensing behaviors between cleanroom wipe and sponge. c) *C–V* measurement of air-gap-based pressure sensor, under various pressure loads. d) Sensing behavior of air-gap pressure sensor. Scale bar of inset digital photo is 3 cm. e) Real-time capacitance change in response to pressure exerted with the bottom of a pen. Scale bar of inset digital photo is 1 cm. f) Peak behavior in response to 12 kPa load. g) Real-time sensing of 32 touch-release cycles. Scale bar of inset digital photo is 1 cm. h) Mutual capacitance effect in response to touch. i) Systolic pressure response when finger is pressed further against the sensor. j) Real-time monitoring of XY plane proximity sensing. k) Proximity sensing plot as a function of approach distance in the z-direction. Scale bar of inset digital photos is 2 cm.

pressure (Figure S5, Supporting Information). This is explained by the thickness of the sponge, which is nearly 12 times thicker than the cleanroom wipe. The results show that the sponge offers 10 times broader pressure detection window, whereas the cleanroom wipe offers six to eight times higher sensitivities in the lower pressure regimes due to its highly deformable microfibril structure.

4.4.2. Real-Time Pressure Detection of the Suspended Air-Gap Structure

We characterize the second capacitive structure fabricated for force sensing (Figure 1e). We study the sensitivity of the sensor by applying small weight loads of PDMS (Figure 5c) and then we perform real-time analysis in response to different external stimuli. Figure 5d shows an exponential growth in response

to pressure. The plot can be divided into two linear regimes where the pressure sensitivity is S_1 = 0.61 pF kPa^{-1} in the low-pressure interval (0–190 Pa), and S_2 = 0.25 pF kPa^{-1} in the high-pressure regime above 200 Pa. To exert higher pressures, we study in Figure 5e the real-time response of the sensor due an applied force of 12 kPa. The pressure response time is measured to be 130 ms and the total recovery time is 13.67 s with an ultrafast half-life time measured to be $t_{1/2}$ = 360 ms (Figure 5f). We record very fast response and recovery times, with pressure sensitivities of 0.11 and 0.044 kPa^{-1} (Figure 5d), comparable or even greater values compared to reported flexible capacitive pressure sensors: 0.23,[59] 0.0004,[60] 0.0002 kPa^{-1}.[61] Although we need to mention that our response time could have been measured to be faster, but was limited to 130 ms due to our sampling rate limitations.

4.4.3. Time Study of Tactile Sensing and Heart Beat Detection

Additionally, we study the effect of a light human touch approaching the air-gap pressure sensing array. Figure 5g shows repetitive cycles of touch and release, where the capacitance exponentially decreases once the sensor is barely touched. This capacitive touch effect is described by the mutual capacitance phenomenon where our finger interferes with the electric field around the capacitor (cross-talk caused by finger) and transfers part of the charge into our conductive and grounded body, hence decreasing the charge collected by the capacitor. Figure 5h illustrates a sharp response to touch, with a total response time ΔT = 911 ms and a total recovery time of 651 ms. And when further pressure is applied with finger (≈3.5 kPa), the capacitance goes up again as depicted in Figure 5i, following a pulsating behavior. The pressure pulse waveform seen reflects the heart beat detection from the pulses originating at the tip of our finger. This pulse corresponds to a capacitance change of 0.71 pF and translated into a pressure pulse detection of 2.84 kPa (Figure 5i), highlighting the efficacy of our device in applications for heart rate and blood pressure monitoring.

4.4.4. Flow Sensing through Low-Pressure Detection

To evaluate the sensor's success in detecting lower pressure regimes, we apply air flows with a variation of flow velocities, translating into various pressures exerted on the surface of our sensor. Figure S6a (Supporting Information) shows the pressure behavior to airflow of v_{normal} = 3 m s^{-1}. The total response time is as fast as 1.04 s, and the total recovery time is only 2.34 s. Based on the detected change in capacitance, our pressure sensor successfully detected an exerted pressure of 82 Pa. We further study the effect of flow angle on the detected pressure. Figure S6b (Supporting Information) shows the pressure response to different flow orientations (0°, 45°, and 90°), for two velocity values: 2 and 8 m s^{-1}. The sensor successfully detected a pressure change even when the air was blown in a tangential manner (0° orientation), with a calculated pressure as low as 9 Pa for a velocity flow of 2 m s^{-1}. As expected, the detected pressure increases as the vector orientation comes closer to the normal direction (Figure S6c, Supporting Information), where all the force vectors become concentrated toward the normal surface of the sensor. The paper-based pressure sensor shows to detect air pressures as low as 9 Pa, with sensitivity to different speeds and flow orientations. Again we need to note that our response to flow detection was limited to 130 ms due to our sampling rate limitation in our measurement tool. In reality, the response time could be much faster.

4.5. Touchless Proximity Sensing

We demonstrate the outstanding proximity sensing capabilities of our capacitive paper-based pressure structure, with 13 cm detection limit as shown in Figure 5j. The principle of operation builds on the principle of electromagnetic (EM) proximity sensing. Upon application of high-frequency sinusoidal signal (f = 1 MHz in this experiment), large EM fields are generated around a capacitor's structure, allowing a conductive object in proximity to interfere with the field and reduce the total charge around the capacitor. The target object can only be a conductor, such as a human finger or body. The EM field generated around the capacitor is further enhanced due to the paramagnetic properties of aluminum foil, allowing a great extension of the field. Thus, as the human finger gets closer to the capacitor, the EM field is disturbed from a far range and the total charge gets redirected from the capacitor toward the detected object, correspondingly decreasing the measured device capacitance. Maxwell's equations provide a complete description of the interactions between charges, currents, electric and magnetic fields. When a magnetic field moves through a conductor (aluminum foil), eddy currents are induced on the surface of the aluminum foil due to the magnetic field's movement. Applying an AC voltage with high frequency to a parallel plate capacitor generates internal electric and magnetic fields in between the two conductive plates. In the most general case, the surface spanned by the integration path of the magnetic field can intercept current and electric flux, and is described by

$$\int_{\text{path}} \vec{\mathrm{B}} \cdot d\vec{\mathrm{L}} = \mu_0 I + \mu_0 \varepsilon_0 \frac{d\varphi_{\mathrm{E}}}{dt} \tag{10}$$

φ_{E} is the electric flux through the surface, B is the magnetic field flux, I is the generated current, ε_0 is the permittivity of free space, and μ_0 is the permeability of free space. Assuming the magnetic field lines inside the capacitor will form concentric circles, then solving for the electric field $\varphi_{\mathrm{E}}(t)$ and the electric flux through the capacitor and the total charge $Q(t)$ on the capacitor, we determine the path integral of the magnetic field around a circle of radius (r) to be equal to

$$\int_{\text{path}} \vec{\mathrm{B}} \cdot d\vec{\mathrm{L}} = 2\pi r B(r) = \mu_0 V_0 \left(\frac{1}{R} \sin(\omega t) + \frac{\varepsilon_0 \pi r^2 \omega}{d} \cos(\omega t) \right) \tag{11}$$

And the strength of the magnetic field (B) [in Tesla] can be finally defined by

$$B(r) = \frac{\mu_0}{2\pi} V_0 \left(\frac{1}{rR} \sin(\omega t) + \frac{\varepsilon_0 \pi r \omega}{d} \cos(\omega t) \right) \tag{12}$$

Our experimental results in Figure 5j show that as we approach the sensor in XY-plane (along z-direction) at a constant rate, the capacitance, respectively, decreases in an exponential fashion, with detection beginning from 13 cm away from the surface of the sensor. *C–V* data were then collected separately for specific proximity distances. Figure 5k illustrates the change in capacitance corresponding to a specific approached distance, from 16 cm down to couple of millimeters. The exponential decrease in capacitance with smaller proximity range displays maximum change in capacitance $\Delta C = 0.55$ pF, corresponding to a detection range of 5 mm. A Video S1 (Supporting Information) of proximity sensing is provided, demonstrating real-time X–Y plane proximity detection.

Our paper-based pressure sensor exhibits exceptional multifunctionality, with notable sensing potentials for pressure, touch, flow, proximity, and directionality. The distinct responses received for pressure, touch, and proximity allow for improved differentiation between multiple mechanical stimuli, enhancing user recognition for touchless control panel applications.

5. Paper Skin Spatiotemporal Mapping

5.1. Simultaneous Mapping of External Stimuli

One major attribute of human skin is simultaneous sensing. To mimic such behavior and for proof-of-concept in large-scale monitoring applications, we demonstrate the spatial real-time mapping of the fabricated 3D stacked paper skin. We simultaneously resolved spatial and temporal information from external stimuli such as touch, pressure, and humid breath to test the skin-like sensing capabilities. To conduct real-time simultaneous sensing on the paper skin, we first started by applying localized human touch, on pixels R3-C3 and R5-C6 and monitored the response from body heat generation. Mapping was done by applying a bias current of 10 mA, and temperature was calculated from the measured resistance change per pixel. **Figure 6**a,b shows the array uniformity and the capability of our paper-based electronic skin to detect the temperature distribution on the pixels generated from the localized finger touch. Real-time temperature monitoring identifies a generated heat of around 34 °C on pixels R3-C3 and R5-C6, which is very close to the temperature of the human body. Some of the surrounding pixels have exhibited a slight increase in temperature (at most +1 °C), which is expected due to heat radiation from the finger. For a second experiment, we simultaneously blew human breath on localized pixels of the paper skin in order to study the capability of identifying separate humidity positions. In order to confine the flow to singular pixels, we used a straw to exert flow on the following pixels: R2-C3, R2-C4, R3-C2, R3-C5, R4-C2, R4-C5, R5-C3, and R5-C4. Figure 6c,d shows humidity matrix distribution and the spatial imaging of applied humidity levels. We can clearly distinguish high humidity levels ranging from 65% to 75% RH, corresponding to the stimulated pixels. As room conditions correspond to 46% RH, we notice that the surrounding pixels were slightly affected with a detected humidity up to 53% RH, a 7% increase in humidity level. Nevertheless, our sensors showed very good performance with an accurate spatial mapping for temperature and humidity.

To conduct pressure mapping using the whole array, first we study the pressure matrix uniformity in Figure 6e, where we observe that the capacitance values vary among pixels from 1.5 pF up to nearly 4 pF, but the majority falls under a capacitance of around 3.5 pF. Then we applied PDMS weights (0.19 g per piece) on specific pixels, ordered in a pattern similar to that of a "chess board." Figure 6f displays the reconstruction of the "chess board" image. Sensed pressures ranged from 0.7 to 1 kPa. This variation in measured pressure values is mainly due to the nonuniformity of the pressure sensing film, underlining the nonuniformity of our array. Moreover, since the sensing film consisted of a common dielectric for all pixels, when one pixel is pressed, neighboring pixels slightly varied. To better illustrate this effect, we plot the 3D bars representation corresponding to localized stimuli (8 kPa load) applied on pixels R1-C2 and R6-C5. Figure 6g displays the 3D mapping image, where we can clearly identify detected pressures in the interval of 0.1–0.4 kPa in the neighboring pixels. This is a very negligible variation ranging from 1% to 5% of the total applied pressure load, highlighting the effective location and load detection of our array. Pressure, temperature, and humidity mapping have all shown robust and concise simultaneous and localized responses.

5.2. 3D Force Trackpad

Finally, we demonstrate the temporal recording of the paper skin and its ability to effectively track motion direction. This was executed by connecting four pixels of the pressure sensor array to an "Arduino Uno" microcontroller, interfaced with "Matlab" software through another code that helped only in reading out the processed information from the serial port. This successfully allowed us to generate and display a real-time histogram plot of the detected movement. A video of the experiment is provided in Video S2 (Supporting Information), where we gently move our finger across four pixels, applying slight pressure, and record the respective change in capacitance with time. Figure 6h illustrates the triggered pixels with time during motion, where we can clearly distinguish separate responses at consecutive times.

We successfully demonstrated a pressure-sensing platform effectively mapping out applied pressure, touch, motion, and proximity, over a large surface area using only paper, cleanroom wipes, and aluminum foil. The demonstrated paper skin could simultaneously measure a variety of external stimuli with great precision. The integration of the proposed sensors did not affect the neighboring sensor's ability to independently distinguish external stimuli, which is translated into negligible external effects on sensor sensitivity. Future work will involve the study of environmental effects such as temperature and ambient humidity changes on the different sensors' parameters. We expect to see slight sensitivity variations due to environmental fluctuations; however simple calibrations can be accounted for to get the appropriate readouts.

6. Artificial Skin Evolution Comparison

Direct comparison between this work and several of the artificial skin platforms being developed by pioneers in the

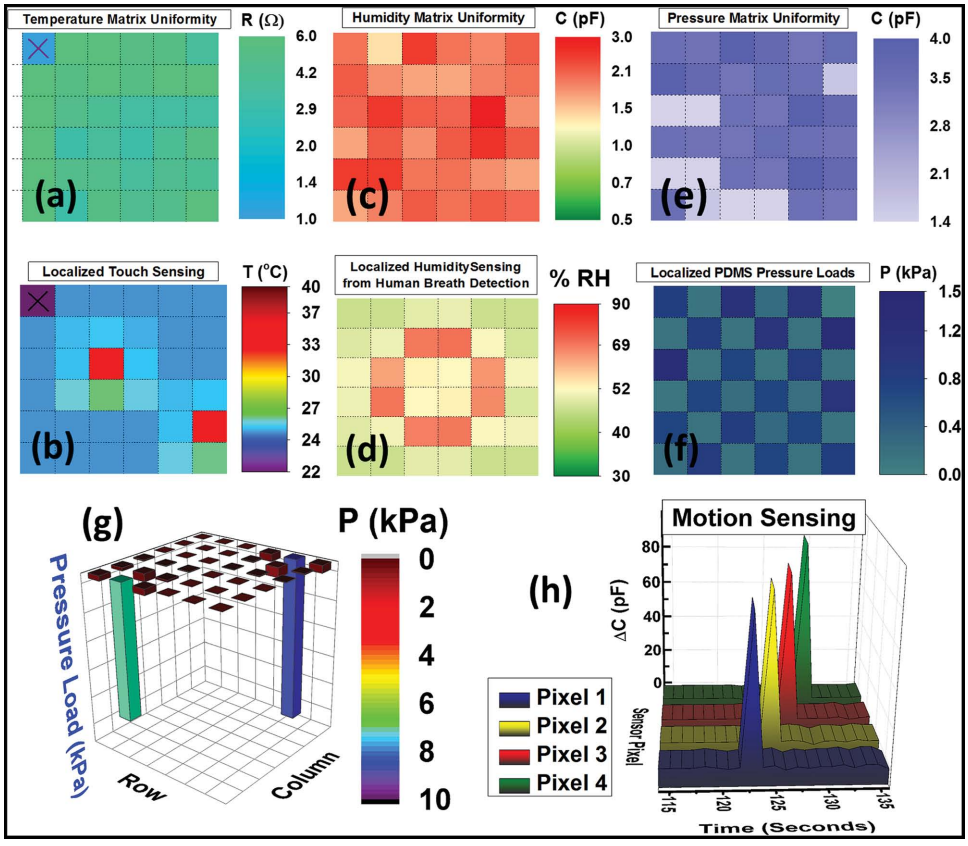

Figure 6. a) Temperature array pixel distribution. Pixel R1-C1 is damaged. b) Spatial mapping of temperature with stimulus exerted on pixels R3-C3 and R5-C6. c) Humidity array pixel-to-pixel uniformity. d) Spatial mapping of humidity in response to stimulus simultaneously applied on pixels R2-C3, R2-C4, R3-C2, R3-C5, R4-C2, R4-C5, R5-C3, and R5-C4. e) Pressure array pixel uniformity. f) Spatial mapping of pressure in a "Chess-board" pattern. g) 3D bars representation corresponding to localized 8 kPa loads on pixels R1-C2 and R6-C5. h) Simultaneous temporal and spatial mapping of motion sensing from four different pixels.

field[1,15,17,22,23,28,29,46,62] shows that our paper skin maintains the desirable high performance of sensors, while displaying more valuable features through the integration of various functionalities with the most affordable materials possible. **Table 1** indicates a summary of the main characteristics found for E-skin platforms based on sensing material used, sensitivity, response time, recovery time, working range, and most importantly cost. Paper skin shows to be clearly the most inexpensive and advantageous option preserving the required high performance of sensors platform.

7. Conclusion

Using only off-the shelf resources, we demonstrated the first ever recyclable paper-based skin capable of detecting temperature, humidity, pH, pressure, touch, flow, motion, and proximity at a record-breaking distance of 13 cm. The fabricated sensors show reliable and consistent results, and the pressure array displayed exceptional capability in differentiating multiple external stimuli. The simplistic fabrication process and low-cost materials used in this work make this flexible platform the lowest cost and accessible to anyone, without affecting performance in terms of response and sensitivity. Additionally, the proximity and motion features obtained in this work illustrate the possibility for paper-based touchless motion systems, bringing the user-to-computer interface experience to a whole new level. Paper skin is an affordable all-in-one flexible sensing platform, applicable for emerging applications, such as health monitoring, 3D touchscreens, and human–machine interfaces, where sensing diversity, surface adaptability, and large-area mapping are all essential. Future works include analysis of performance characteristics and reliability of the fabricated skin under various mechanical deformations (flexing, stretching, etc.). Although further sophistication is possible, at the present stage the demonstrated "paper skin" integrates the maximum sensory functions of a human skin in a cost effective and eco-friendly manner.

8. Experimental Section

Temperature Design: Sensors using silver ink pen have a 1 × 1 cm^2 resistor structure drawn directly on Post-it paper with resistor line width of 1 mm and 1 mm line separation. Sensors made out of aluminum foil are simply 3 × 1 cm^2 resistor structure cut from the foil sheet, with 2 mm line width, and 2 mm line separation.

Humidity Design: 1 × 1 cm^2 interdigitated electrodes structure using silver ink pen, with 2 mm finger width and 1 mm finger separation. Then

Table 1. Summary of E-skin sensors characteristics. Table comparing this work to several artificial skin platforms, displaying differentiation between performance, material, functionality, and cost.

Reference	Functionality	Sensing material	Sensitivity	Response time	Recovery time	Working Range	Cost
Biological skin[62]	Force	N.A.	0.018–0.078 [kPa^{-1}]	30–50 ms	<2 kPa	N.A.	–
Takei[15]	Temperature	CNT-PEDOT:PSS on PET	0.0025 [°C]	1 s	19 s	N.A.	↑
	Strain/Pressure	AgNP-CNT on PE	0.13 [mN]	2.5 s	22 s	N.A.	↑
Bao[17,23]	Pressure[3]	PDMS	0.025–0.2 [kPa^{-1}]	2.5 s	300 ms	0–35 [kPa]	←
	Temperature[4]	P(VDF-TrFE) & BaTiO3 NPs	N.A.	2.5 s	N.A.	N.A.	↑
Javey[28,29]	Pressure	CNTs; NWs	0.09 kPa^{-1}; 0.033 kPa^{-1}	2.5 s	<0.1 s	<6 kPa; 2–15 [kPa]	↑
Fang[46]	Humidity	RF-aerogels	0.56%/%RH	2.5 s	N.A.	N.A.	↑
D-H Kim[22]	Pressure/strain	Si nanoribbons (SiNR)	0.0041 [kPa^{-1}]	2.5 s	N.A.	N.A.	↑
Han[1]	Humidity	COOH-functionalized SWCNTs on cellulose paper	0.06%/%RH	2.5 s	120 s	N.A.	↑
This Work	Temperature	Silver ink pen	0.00372 [°C]	2.5 s	5.3 s	N.A.	←
		Aluminum foil	0.00383 [°C]	N.A.	N.A.	N.A.	↓
	Humidity	Post-it note paper	0.18%/%RH	1.2 s	1.33 s	Full range of RH	↓
	Force (pressure, tactile, flow sensing)	Cleanroom napkin/sponge	0.16 [kPa^{-1}]	<130 ms[a)]	<130 ms[a)]	>0.009 [kPa]	↓
	Proximity	Aluminum foil	N.A.	N.A.	N.A.	13 cm away	↓

[a)]These response and recovery times are limited by our tool temporal resolution, with a sampling rate of 130 ms per data point. In reality, the behavior of our signal shows that these numbers should be significantly lower as reported in main text.
↑ Highly costly; ↓ Very low-cost; ← Relatively average cost.

the surface was protected with a 1.5 × 1.5 cm^2 sheet of Kimtech wipe, taping the edges on the paper substrate using 3M adhesive tape. Paper acted as the sensing film and the substrate.

PH Design: Paper acted only as the flexible substrate. Interdigitated electrodes were outlined with the silver conductive pen, with 3 mm finger width and 2 mm finger separation. After it was completely dried, a 3 × 3 cm^2 sheet was drawn of sensing film using a graphite pencil of grade HB. It was made sure that the layer was uniformly distributed and colored.

Pressure Design—Two Structures: (1) Simple parallel plate capacitor structure. Paper used as a substrate for keeping the final structure flat and stable. Then, a 1 × 1 cm^2 sheet of aluminum foil was deposited, taped on the paper using 1 × 1 cm^2 sheet of double-sided tape. Then, another layer of double-sided tape (d_{tape} = 90 µm) was deposited to attach the dielectric material on top. Two different dielectric materials were used: a porous sponge (d_{sponge} = 0.7 cm) and 100% PP microfiber cleanroom wipe ($d_{fiber\text{-}wipe}$ = 600 µm) (Berkshire PRO-WIPE 880). Finally, again a layer of double-sided adhesive tape was deposited to fix the 1 × 1 cm^2 aluminum foil top electrode. (2) Air-gap suspended design. A 90 µm air gap was introduced into the first pressure structure described above. Air gap is created through anchors on either side of the sensor: after depositing the first metal electrode, two double-sided tape stripes of 2 mm width were placed on the either edge of the capacitor.

Paper Skin Array—3D Stacked 6 × 6 Arrays: Three layers of sensors arrays were overlaid on top of each other. Each layer was composed of one sensor type, with 1 cm^2 pixel size and 1 mm edge to edge pixel separation. Layer 1 consisted of air-gap pressure sensors: bottom electrode acted as a common ground for all pixels, and the shared dielectric consisted of a large 11 × 11 cm^2 cleanroom wipe sheet. Layer 2 consisted of an array of silver-ink-based temperature sensors. Layer 3 was an array of humidity sensors with an optional protective KIMTECH wipe on top. The three layers are stacked in such a way that pressure, temperature, and humidity pixels were exactly on top of each other. Singular pixels can be independently accessed, allowing for simultaneous localized sensing.

Real-Time Measurements: Sensors were tested using Keithley 4200 interface capable of real-time voltage and capacitance measurements. CV extracted by applying 1 MHz modulation frequency and 100 mV AC voltage. Sampling rate was limited by the tool to 130 ms/data point, given that we were running in "Quiet" mode in order to reduce noise interference.

Water Vapor Setup: Tap water was boiled in a beaker glass and brought it in proximity to our sensor (Figure 4h). To direct the water vapor toward the sensor, a wind tunnel setup was used. The attached fan was installed in a way to suck the air from the sensor side toward the wind tunnel in a laminar manner, allowing the humid air to flow across the surface of our sensor (Figure 4i).

Flow Detection Setup: Compressed air was flown through a 1 mm diameter nozzle. Normal flow velocities were measured using a digital anemometer of 0.1 m s^{-1} accuracy. The specified velocity magnitudes were that of a normal velocity vector, normal to the sensor's plane (90° orientation). Flow orientation was determined using a protractor.

Proximity Setup: For distance evaluation, a ruler was vertically installed next to our sensor (along z-direction), making sure that the zero value of the ruler corresponded to the surface level of our pressure sensor.

Supporting Information

Supporting Information is available from the Wiley Online Library or from the author.

Acknowledgements

We thank Swanlund Chair Prof. John Rogers at University of Illinois, Urbana-Champaign for useful discussion about this paper.

Received: January 15, 2016
Published online: February 19, 2016

[1] J.-W. Han, B. Kim, J. Li, M. Meyyappan, *RSC Adv.* **2014**, *4*, 549.
[2] H. Koga, M. Nogi, N. Komoda, T. T. Nge, T. Sugahara, K. Suganuma, *NPG Asia Mater.* **2014**, *6*, e93.
[3] J. Lessing, A. C. Glavan, S. B. Walker, C. Keplinger, J. A. Lewis, G. M. Whitesides, *Adv. Mater.* **2014**, *26*, 4677.
[4] A. Russo, B. Y. Ahn, J. J. Adams, E. B. Duoss, J. T. Bernhard, J. A. Lewis, *Adv. Mater.* **2011**, *23*, 3426.
[5] A. C. Siegel, S. T. Phillips, B. J. Wiley, G. M. Whitesides, *Lab Chip* **2009**, *9*, 2775.
[6] D. Tobjörk, R. Österbacka, *Adv. Mater.* **2011**, *23*, 1935.
[7] E. L. Tan, W. N. Ng, R. Shao, B. D. Pereles, K. G. Ong, *Sensors* **2007**, *7*, 1747.
[8] T. Unander, H.-E. Nilsson, *IEEE Sens. J.* **2009**, *9*, 922.
[9] L. Wang, W. Chen, D. Xu, B. S. Shim, Y. Zhu, F. Sun, L. Liu, C. Peng, Z. Jin, C. Xu, *Nano Lett.* **2009**, *9*, 4147.
[10] S. Yun, J. Kim, *Sens. Actuators, B.* **2010**, *150*, 308.
[11] A. Manzoli, C. Steffens, R. T. Paschoalin, A. A. Correa, W. F. Alves, F. L. Leite, P. S. Herrmann, *Sensors* **2011**, *11*, 6425.
[12] J. Jang, J. Ha, J. Cho, *Adv. Mater.* **2007**, *19*, 1772.
[13] V. Lakafosis, A. Rida, R. Vyas, L. Yang, S. Nikolaou, M. M. Tentzeris, *Proc. IEEE* **2010**, *98*, 1601.
[14] M. L. Hammock, A. Chortos, B. C. K. Tee, J. B. H. Tok, Z. Bao, *Adv. Mater.* **2013**, *25*, 5997.
[15] S. Harada, K. Kanao, Y. Yamamoto, T. Arie, S. Akita, K. Takei, *ACS Nano* **2014**, *8*, 12851.
[16] S. Park, H. Kim, M. Vosgueritchian, S. Cheon, H. Kim, J. H. Koo, T. R. Kim, S. Lee, G. Schwartz, H. Chang, *Adv. Mater.* **2014**, *26*, 7324.
[17] G. Schwartz, B. C.-K. Tee, J. Mei, A. L. Appleton, D. H. Kim, H. Wang, Z. Bao, *Nat. Commun.* **2013**, *4*, 1859.
[18] J. Y. Sun, C. Keplinger, G. M. Whitesides, Z. Suo, *Adv. Mater.* **2014**, *26*, 7608.
[19] X. Wang, Y. Gu, Z. Xiong, Z. Cui, T. Zhang, *Adv. Mater.* **2014**, *26*, 1336.
[20] L. Gao, Y. Zhang, V. Malyarchuk, L. Jia, K.-I. Jang, R. C. Webb, H. Fu, Y. Shi, G. Zhou, L. Shi, *Nat. Commun.* **2014**, *5*, 4938.
[21] X. Huang, Y. Liu, H. Cheng, W. J. Shin, J. A. Fan, Z. Liu, C. J. Lu, G. W. Kong, K. Chen, D. Patnaik, *Adv. Funct. Mater.* **2014**, *24*, 3846.
[22] J. Kim, M. Lee, H. J. Shim, R. Ghaffari, H. R. Cho, D. Son, Y. H. Jung, M. Soh, C. Choi, S. Jung, *Nat. Commun.* **2014**, *5*, 5747.
[23] M. Ramuz, B. C. K. Tee, J. B. H. Tok, Z. Bao, *Adv. Mater.* **2012**, *24*, 3223.
[24] M. Segev-Bar, A. Landman, M. Nir-Shapira, G. Shuster, H. Haick, *ACS Appl. Mater. Interfaces* **2013**, *5*, 5531.
[25] T. Sekitani, T. Someya, *Adv. Mater.* **2010**, *22*, 2228.
[26] T. Someya, *Spectrum IEEE* **2013**, *50*, 50.
[27] T. Someya, Y. Kato, T. Sekitani, S. Iba, Y. Noguchi, Y. Murase, H. Kawaguchi, T. Sakurai, *Proc. Natl. Acad. Sci. USA* **2005**, *102*, 12321.
[28] T. Takahashi, K. Takei, A. G. Gillies, R. S. Fearing, A. Javey, *Nano Lett.* **2011**, *11*, 5408.
[29] K. Takei, T. Takahashi, J. C. Ho, H. Ko, A. G. Gillies, P. W. Leu, R. S. Fearing, A. Javey, *Nat. Mater.* **2010**, *9*, 821.
[30] N. T. Tien, S. Jeon, D. I. Kim, T. Q. Trung, M. Jang, B. U. Hwang, K. E. Byun, J. Bae, E. Lee, J. B. H. Tok, *Adv. Mater.* **2014**, *26*, 796
[31] C. Wang, D. Hwang, Z. Yu, K. Takei, J. Park, T. Chen, B. Ma, A. Javey, *Nat. Mater.* **2013**, *12*, 899.
[32] C. R. Nave, Resistor Temperature Dependence, http://hyperphysics.phy-astr.gsu.edu/hbase/electric/restmp.html (accessed June 2015).
[33] N. Yamazoe, Y. Shimizu, *Sens. Actuators* **1986**, *10*, 379.
[34] Queensland Curriculum & Assessment Authority QCAA, Extended Experimental Investigation: Electrical Conductivity of Graphite, https://www.qcaa.qld.edu.au/downloads/senior/snr_physics_07_sai_electric_conduct_graphite.pdf (accessed June 2015).
[35] P. Geissler, C. Dellago, D. Chandler, J. Hutter, M. Parrinello, *Science* **2001**, *291*, 2121.
[36] M. R. Leach, The Chemogenesis Web Book: Redox Chemistry, http://www.metasynthesis.com/webbook/15_redox/redox.php (accessed December 2015).
[37] Y. Zang, F. Zhang, D. Huang, X. Gao, C.-A. Di, D. Zhu, *Nat. Commun.* **2015**, *6*, 6269.
[38] S. Jung, J. H. Kim, J. Kim, S. Choi, J. Lee, I. Park, T. Hyeon, D. H. Kim, *Adv. Mater.* **2014**, *26*, 4825.
[39] N. Balasubramanian, P. v. Polypropylene. http://www.fibre2fashion.com/industry-article/textile-industry-articles/polyester-vs-polypropylene/polyester-vs-polypropylene1.asp (accessed June 2015).
[40] C. Tomizuka, E. Sonder, *Phys. Rev.* **1956**, *103*, 1182.
[41] A. Technologies, *Material Expansion Coefficients: Linear Thermal Expansion Coefficients of Metals and Alloys*, Material Expansion Coefficients, Agilent Technologies, Santa Clara, CA, USA **2002**.
[42] P. Mürtz, L. Menzel, W. Bloch, A. Hess, O. Michel, W. Urban, *J. Appl. Physiol.* **1999**, *86*, 1075.
[43] S. M. Abdullah, Z. Ahmad, K. Sulaiman, *Sensors* **2014**, *14*, 9878.
[44] L. Gu, Q.-A. Huang, M. Qin, *Sens. Actuators B* **2004**, *99*, 491.
[45] C.-Y. Lee, W.-J. Hsieh, G.-W. Wu, *J. Power Sources* **2008**, *181*, 237.
[46] V. P. Chung, C.-L. Cheng, M.-C. Yip, W. Fang, in *28th IEEE Int. Conf. Micro Electro Mech. Syst.*, IEEE, Piscataway, NJ, USA **2015**, 767.
[47] C.-H. Lin, L.-M. Fu, C.-Y. Lee, in *9th IEEE Int. Conf. Nano/Micro Eng. Mol. Syst.*, IEEE, Piscataway, NY, USA **2014**, 191.
[48] T. Yang, Y. Yu, L. Zhu, X. Wu, X. Wang, J. Zhang, *Sens. Actuators, B* **2015**, *208*, 327.
[49] D. Shou, L. Ye, J. Fan, K. Fu, *Langmuir* **2013**, *30*, 149.
[50] J. Cai, B. Yu, M. Zou, L. Luo, *Energy Fuels* **2010**, *24*, 1860.
[51] D. Dimitrov, A. Milchev, K. Binder, *Phys. Rev. Lett.* **2007**, *99*, 054501.
[52] R. Griffiths, I. Roberts, *Atmos. Environ.* **1999**, *33*, 3531.
[53] M. Matalon, Princeton Lecture 13: Droplet Combustion and Spray Modeling, https://www.princeton.edu/cefrc/Files/2011%20Lecture%20Notes/Matalon/Lecture-13.pdf (accessed January 2016).
[54] H. Chraibi, M. Prat, O. Chapuis, *Phys. Rev. E* **2009**, *79*, 026313.
[55] A. Yiotis, A. Boudouvis, A. Stubos, I. Tsimpanogiannis, Y. Yortsos, *AIChE J.* **2004**, *50*, 2721.
[56] T. Hizawa, K. Sawada, H. Takao, M. Ishida, *Sens. Actuators, B* **2006**, *117*, 509.
[57] N. Lei, P. Li, W. Xue, J. Xu, *Meas. Sci. Technol.* **2011**, *22*, 107002.
[58] N. F. Sheppard, M. J. Lesho, P. McNally, A. S. Francomacaro, *Sens. Actuators, B* **1995**, *28*, 95.
[59] X. Liu, Y. Zhu, M. W. Nomani, X. Wen, T.-Y. Hsia, G. Koley, *J. Micromech. Microeng.* **2013**, *23*, 025022.
[60] D. P. Cotton, I. M. Graz, S. P. Lacour, *IEEE Sens. J.* **2009**, *9*, 2008.
[61] D. J. Lipomi, M. Vosgueritchian, B. C. Tee, S. L. Hellstrom, J. A. Lee, C. H. Fox, Z. Bao, *Nat. Nanotechnol.* **2011**, *6*, 788.
[62] V. Arumugam, M. Naresh, R. Sanjeevi, *J. Bio Sci.* **1994**, *19*, 307.